5-15-2015

Lower Thermospheric Response to Atmospheric Gravity Waves Induced By the 2011 Tohoku Tsunami

Yonghui Yu
College of Astronautics; Nanjing Univeristy of Aeronautics and Astronautics, yuyong@nuaa.edu.cn

Zhiyu Yan
College of Astronautics; Nanjing University of Aeronautics and Astronautics

Michael P. Hickey Ph.D.
Embry-Riddle Aeronautical University, hicke0b5@erau.edu

AGU PUBLICATIONS

JGR

Journal of Geophysical Research: Space Physics

RESEARCH ARTICLE
10.1002/2015JA020986

Key Point:
- Travel speeds of tsunami outward from epicenter are azimuthally anisotropic
- Tsunamigenic atmospheric gravity waves have anisotropic distribution of phase speeds
- Atmospheric mean winds can amplify wave upward propagation characteristics

Correspondence to:
Y. Yu,
yuyong@nuaa.edu.cn

Citation:
Yu, Y., Z. Yan, and M. P. Hickey (2015), Lower thermospheric response to atmospheric gravity waves induced by the 2011 Tohoku tsunami, *J. Geophys. Res. Space Physics*, *120*, doi:10.1002/2015JA020986.

Received 6 JAN 2015
Accepted 13 MAY 2015
Accepted article online 15 MAY 2015

Lower thermospheric response to atmospheric gravity waves induced by the 2011 Tohoku tsunami

Yonghui Yu[1], Zhiyu Yan[1], and Michael P. Hickey[2]

[1]College of Astronautics, Nanjing University of Aeronautics and Astronautics, Nanjing, China, [2]Department of Physical Sciences, Embry-Riddle Aeronautical University, Daytona Beach, Florida, USA

Abstract Previous GPS observations have revealed that while ionospheric TIDs were seen propagating in all directions away from the 2011 Tohoku earthquake epicenter, the total electron content (TEC) fluctuations associated with the subsequent tsunami were largest for waves propagating toward the northwest of the epicenter. Ionospheric motions observed approximately 10 min after the earthquake were attributed to fast acoustic waves directly produced by the earthquake. Waves that first appeared about 40 min after the tsunami onset in TEC measurements were attributed to atmospheric gravity waves. In this paper, we conjecture that the remarkably different responses observed for the eastward and westward propagating waves noted in previous observations can be explained by the different ocean depths associated with the two directions of travel and by the effects of the mean winds. The former has consequences for the generated gravity waves (wave spectrum), while their combination has consequences for the ability of the waves to propagate to higher altitudes. Because the ocean depth to the east of the epicenter is greater than that to the west, the eastward propagating tsunami travels faster than the westward propagating tsunami; and hence, the eastward propagating gravity waves that are generated will be faster than the westward waves. We demonstrate that the faster eastward waves encounter regions of evanescence that inhibits their upward propagation, with the result that the westward propagating waves reach the lower thermosphere sooner and with much larger amplitudes than those of the eastward propagating waves. However, at much higher altitudes the slower westward propagating waves are severely damped by viscosity, with the result that only the eastward propagating waves survive to *F* region altitudes. These results are clearly seen in our full-wave model simulations and also in the evolution of the wave momentum flux calculated using our 2-D, time-dependent model.

1. Introduction

The Tohoku tsunami was generated by an earthquake that occurred at 5 h 46 m (UT) (14:46 JST) on 11 March 2011 and had a moment magnitude of about 8.9. The epicenter was located at 38.322°N and 142.369°E, approximately 70 km off the east coast of Japan. The resulting tsunami propagated away from the epicenter in all directions across the Pacific Ocean and resulted in tremendous damage to Japan. The massive amount of tsunami debris that has been floating in the Pacific Ocean for the last few years still continues to occasionally appear on the west coast of the USA. However, the earthquake led to more than just ocean waves (the tsunami); through coupling with the atmosphere, the tsunami generated upward propagating atmospheric disturbances which reached the upper atmosphere and were subsequently detectable with GPS receivers by the radio scientific community [e.g., *Galvan et al.*, 2012; *Komjathy et al.*, 2012].

Tsunamis are long oceanic gravity waves usually excited by underwater earthquakes. Because their horizontal wavelengths are considerably greater than the ocean depth (~4 km for the Pacific Ocean), they propagate at speeds approximately equal to the shallow-water wave speed (~200 m/s). Additionally, because their characteristic scales (periods tens of minutes and wavelengths hundreds of kilometers) lie within the range of medium scale atmospheric gravity waves, the coupling between tsunamis and atmospheric gravity waves is expected to be strong, suggesting that a tsunami could be an efficient source of atmospheric gravity waves [*Hines*, 1972].

In the past, several authors have modeled or reported atmospheric gravity waves driven by tsunamis. *Peltier and Hines* [1976] first modeled the idealized atmospheric response to an idealized tsunami. Their studies supported the plausibility of tsunami-generated atmospheric gravity waves propagating upward into the ionosphere. *Artru et al.* [2005a] reported observations of a traveling ionospheric disturbance (TID)

following a tsunami generated by the Peruvian earthquake of 23 June 2001. Later, *Artru et al*. [2005b] analyzed total electron content (TEC) measurements obtained from the GPS Earth Observation Network (GEONET) in Japan to study ionospheric perturbations following the same tsunami. *Occhipinti et al*. [2008] simulated the effects of different latitudes and directions of wave propagation on the ionospheric response to the 2004 Sumatra tsunami. Recently, *Hickey et al*. [2009, 2010a] have modeled a spectrum of gravity waves and corresponding airglow responses driven by the 2004 Sumatra tsunami propagating into the thermosphere and ionosphere, and shown that significant acceleration of the atmosphere could occur in the middle thermosphere as a result of the momentum deposition associated with the dissipation of the gravity waves [*Hickey et al*., 2010b].

The Tohoku tsunami occurred in a region that was densely populated by a network of GPS receivers, which meant that the ionospheric response to the earthquake/tsunami could be studied in unprecedented detail. One set of TEC observations reported by *Galvan et al*. [2012] revealed that within the first hour following the tsunami onset, more enhanced TID activity occurred which was presumably associated with the underlying gravity waves. Although their TEC measurements (shown in their Figure 2) indicate ionospheric TIDs occurring in all directions around the epicenter, the TID activity to the west and northwest of the epicenter was particularly enhanced, while activity to the east was minimal (although we remark that the GPS network to the east is quite sparsely populated compared to the west).

Galvan et al. [2012] conjectured that the westward traveling tsunami would have an increasing amplitude as it approached the coast due to the decreasing water depth, which in turn would generate larger amplitude atmospheric waves. Here we examine an alternative and plausible explanation for the apparently stronger waves traveling toward the west and northwest. The tsunami speed, a function of water depth, will be azimuthally anisotropic, which means that the generated atmospheric waves should also have an anisotropic distribution of phase speeds with azimuthal direction. Hence, as the waves propagate obliquely upward, their propagation characteristics will be different for the different directions of propagation. Furthermore, these differences will also be amplified by the effects of the mean winds. We should add that the wave amplification that occurs due to decreasing water depth as discussed by *Galvan et al*. [2012] will also be an important factor for the westward and northwestward propagating waves, though we do not consider that in this paper.

The purpose of the paper is to quantitatively evaluate the atmospheric response to the atmospheric gravity waves driven by the 2011 Tohoku tsunami in order to determine how the wave amplitudes differ for the different directions of propagation. First of all, an analysis of a primary wave amplitude and phase varying with altitudes is performed in a nonisothermal atmosphere with viscosity and in the presence of background winds. Second, in order to trace the upward movement and evolution of the wave packet from the ocean surface to the mesosphere and lower thermosphere (MLT), the vertical flux of wave horizontal momentum evolution with height and time is also presented. A 1-D linear, steady state full-wave model and a 2-D nonlinear, time-dependent model are used in the current numerical simulations. The paper is organized as follows. The undisturbed mean state of the atmosphere in the vicinity of the earthquake is described in section 2. The numerical models and appropriate input parameters are described in section 3. The results of the simulations are provided in section 4 and are further discussed in the discussion section (section 5). Conclusions are presented in section 6. The 2-D model equations and the viscosity and thermal conductivity profiles it employs are described in Appendix A.

2. Undisturbed Mean State

The mean atmosphere is defined here using the MSIS-90 model [*Hedin*, 1991] for conditions predominating at the epicenter and at the time of the 2011 Tohoku tsunami, for a latitude and longitude of 38.322°N and 142.369°E, respectively, and for a universal time of 0546 h on 11 March. The solar $F_{10.7}$ index and its 81 day mean are chosen to be 88.7 and 102.8, respectively, appropriate to the time of the tsunami. The geomagnetic index $ap = 12$. The horizontal mean winds are described here by the HWM93 model [*Hedin et al*., 1996] using these same inputs.

The mean horizontal winds can significantly affect wave propagation and transmission through the atmosphere and hence lead to the anisotropic propagation of the waves. Figure 1a shows that the meridional wind (positive southward) is approximately within the range between −12 m/s and 42 m/s below 140 km

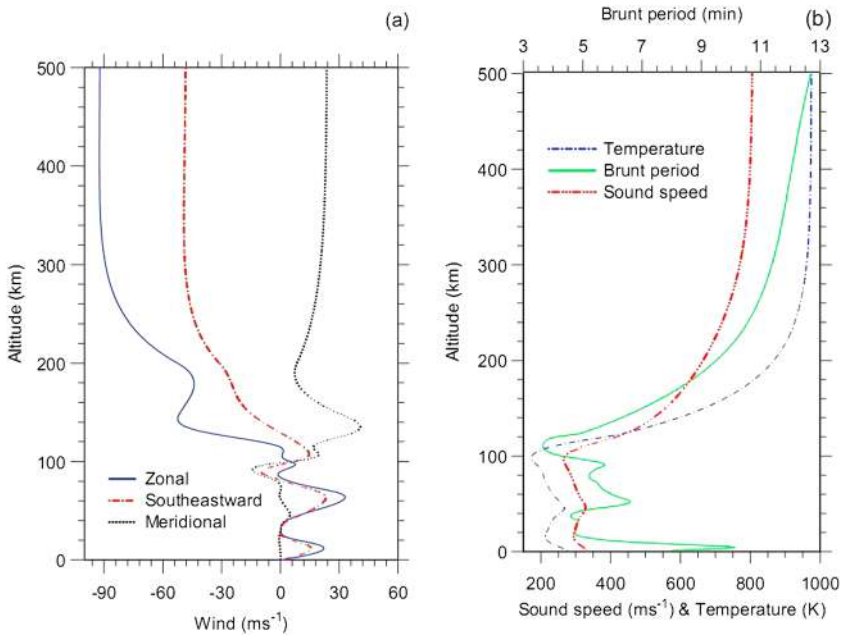

Figure 1. (a) Horizontal mean winds (positive eastward, southeastward, and southward), (b) Brunt-Väisälä period (upper *x* axis), sound speed, and mean temperature (lower *x* axis) near the epicenter.

altitude. Above that it decreases slightly and then asymptotes to about 24 m/s in the southward direction by 500 km altitude. The zonal wind (positive eastward) is approximately within the range between 0 and 30 m/s eastward up to the turbopause (105 km), and then, except for a slight decrease between about 140 and 200 km altitude, it generally increases smoothly in the westward direction between about 100 and 300 km altitude. At greater heights, it asymptotes to a westward speed of about 90 m/s by 500 km altitude. Based on the meridional and zonal winds, we also show the mean wind in the southeast direction (defined as positive). The southeastward wind lies within the range between about −12 m/s and 24 m/s up to 100 km altitude, and approaches a northwestward value of about 48 m/s by 500 km altitude.

Figure 1b shows the altitude variations of the mean temperature and the Brunt-Väisälä period. The mean temperature achieves an exospheric temperature of about 975 K at high thermospheric altitudes. The Brunt-Väisälä period has a local minimum of slightly greater than 4.5 min near 40 km altitude and slightly less than 4 min around 110 km altitude. Hence, waves of about 4 min to 4.5 min period will be evanescent throughout the atmosphere. Above about 120 km altitude, the Brunt-Väisälä period increases with increasing altitude. Because internal gravity waves necessarily exist at periods longer than this, progressively more of the shorter period waves are removed during the upward propagation of a gravity wave packet. Near the *F* region peak (300 km), the Brunt-Väisälä period is about 11.5 min, so waves of period longer than this are expected to dominate the *F* region response to an upward propagating wave packet. The sound speed, also shown in this figure, has local minima near 18 km and 100 km altitude, with values of approximately 300 m/s and 280 m/s, respectively. In the upper thermosphere, it asymptotes to a value of about 800 m/s.

3. Numerical Models and Input Parameters

The 2011 Tohoku tsunami occurred in response to an earthquake having its epicenter located at 38.322°N and 142.369°E, and located on the North American Plate approximately one third of the way between the east coast line of Japan and the center of the Japan Trench in a southeastward direction. The center depth of the Japan Trench is about 7.4 km. Eastward and southeastward of the epicenter the ocean becomes quite deep, while westward and northwestward of the epicenter (approaching the east coast of Japan) the ocean becomes shallower. The relative location of the epicenter is shown on the ocean map provided (Figure A1). The tsunami travels in all directions at the local shallow-water wave speed, $\sqrt{gh}$, where g is the acceleration due to gravity and h is the ocean depth.

Galvan et al. [2012] provided some useful geographic parameters used in our simulations, which are summarized as follows. For propagation toward the northwest and the west, where the average depth is 1.5 km, the estimated shallow-water wave speed is 121 m/s. For propagation toward the east, where the average depth is 5 km, the estimated shallow-water wave speed is 221 m/s. Ocean buoys in NOAA's DART network (Deep-ocean Assessment and Reporting of Tsunamis) measure the average tsunami speed between the epicenter and the buoy location. For example, DART buoy # 21419 measured an average wave speed of 243 m/s southeast of the epicenter, consistent with an estimated average depth of 6025 m (less than 7400 m at the center of the Japan Trench). The wave amplitude of about 0.76 m derived from the sea surface height and a wave period of about 32 min are another two important parameters provided by DART [*Galvan et al*., 2012].

Two numerical models are used here in order to study the propagation of atmospheric gravity waves from the lower atmosphere to the lower thermosphere (and the *E* region ionosphere). The first model is a linear steady state full-wave model which has been described previously by *Hickey et al*. [1997]. It has been used extensively since then by *Hickey* and colleagues to interpret acoustic-gravity waves [e.g., *Hickey and Yu*, 2005], and to study tsunami-driven gravity wave propagation and dissipation in the terrestrial atmosphere using a spectral approach [e.g., *Hickey et al*., 2009, 2010a, 2010b]. The full-wave model solves the complete linearized equations of continuity, momentum, and energy for a compressible, viscous, and thermally conducting atmosphere with an arbitrary altitude variation in a thermal and windy structure of the basic state. The model produces altitude profiles of the complex fluctuations of horizontal and vertical velocities, temperature, and pressure, which we represent by their amplitudes and phases. The high-resolution model domain extends from the ground to 500 km altitude with 100,000 grid points. The monochromatic 32 min wave is forced at the lower boundary (sea level) of the full-wave model with vertical velocity amplitude of 2.49×10^{-3} m/s ($=\omega\xi$, where ω is the wave frequency and ξ is the maximum surface displacement).

The second model is a 2-D time-dependent, nonlinear model [*Yu and Hickey*, 2007a, 2007b, 2007c; *Yu et al*., 2009]. Details of this model are provided in Appendix A. For the 2011 Tohoku tsunami, the prescribed source of the vertical displacement ξ, at the lower boundary (sea level) of the 2-D model, is applied to the right-hand side of the vertical momentum equation (A1, in Appendix A) and is described analytically as a traveling sinusoidal wave modulated by a Gaussian envelop over time, as follows:

$$\xi(x,0,t) = 0.76 \times \exp\left(-(t-\tau)^2/2\Delta t^2\right)\sin(k_0 x - \omega_0 t). \quad (1)$$

Here x is the horizontal position, and t is the time. The half width Δt is equal to 16 min for $t \leq 46$ min and 32 min for $t > 46$ min, t is centered at time $\tau = 46$ min and coincident with the 2011 Tohoku tsunami onset at 05:46 UT. The dominant wave of 32 min period measured by DART [*Galvan et al*., 2012] suggests that a half width of 32 min be used after the center time (46 min), and half of this value (16 min) be used before the center time in order to provide a ramp that approximates the rising displacement of the sea surface and mimics a sudden emergence of the tsunami. The remaining parameters of the wave source are $\omega_0 = 2\pi/\tau_w$ where the period τ_w is 32 min, and $k_0 = 2\pi/\lambda_h$ where the horizontal wavelength λ_h (and associated phase speed) is 424.32 km (221 m/s), 232.32 km (121 m/s), 232.32 km (121 m/s), and 466.56 km (243 m/s) for the eastward, westward, northwestward, and southeastward propagation direction, respectively. These prescribed source configurations are applied in the 2-D nonlinear, time-dependent model and implemented using four separate model simulations, one for each propagation direction.

4. Results of Simulation

Figure 2 shows the temporal evolution of the ocean surface displacement at the epicenter due to the simulated tsunami. It is characterized by a rapid rise in amplitude within two primary wave periods, and followed by two or more periodic trailing waves of diminishing amplitude. An analysis of the prescribed source configuration in equation (1) is consistent with the maximum amplitude (0.76 m) occurring between the time of 40 and 60 min. Also shown in this figure is the corresponding normalized spectral amplitude as a function of wave period. The spectral amplitude is obtained by using the fast Fourier transform applied to the time series of the sea surface displacement (ξ, equation (1)). It has been normalized by partitioning a fraction of the total power amplitude for each wave component. Most gravity wave components lie within the range between 20 min and 60 min. The maximum of the normalized spectral amplitude is about 0.42 for the primary 32 min wave period.

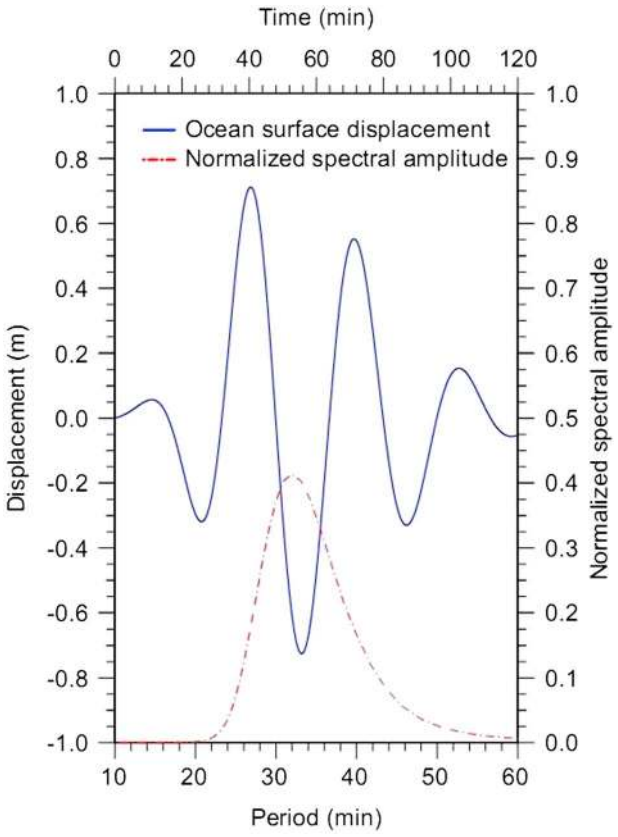

Figure 2. Ocean surface displacement (solid line, upper *x* axis, left *y* axis) and normalized spectral amplitude (dashed dotted line, lower *x* axis, right *y* axis) at the epicenter.

The refractive index (m^2, where m is the vertical wave number calculated using the nonisothermal dispersion relation of *Einaudi and Hines* [1971]) obeys the approximate dispersion equation for low-frequency gravity waves (in our case, for the 32 min period waves),

$$m^2 \approx \frac{N^2}{c^2} - \frac{{\omega_a}^2}{{C_s}^2}. \quad (2)$$

It is straightforward to show that the maximum phase speed, c_{max}, for internal wave propagation is given by $c_{max} \approx 2HN$ [*Walterscheid and Hickey*, 2011]. Here H is the atmospheric scale height, N is the Brunt-Väisälä frequency, c is the intrinsic phase speed with respect to a frame reference moving with the background wind, C_s is the sound speed, and $\omega_a = C_s/(2H)$ is the acoustic cutoff frequency. For an isothermal atmosphere $c_{max} \approx 0.93C_s$, but for a nonisothermal atmosphere and for conditions appropriate to the troposphere $c_{max} \approx 0.54C_s$ (≈150 m/s in the midtroposphere).

The refractive indexes for the 32 min gravity waves are shown as a function of height in Figure 3. The eastward propagating wave

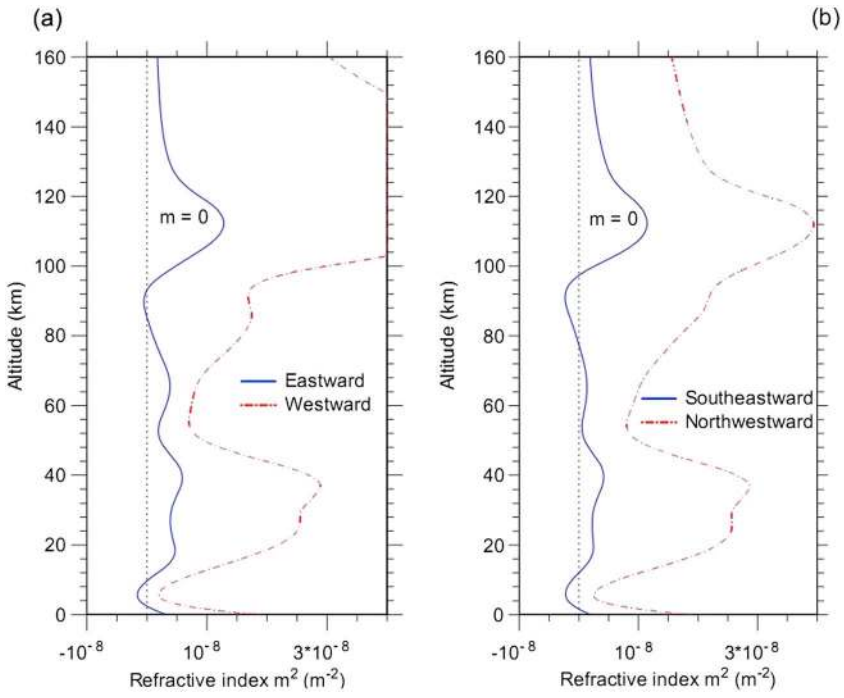

Figure 3. Refractive indexes for the 32 min waves propagating (a) in the eastward and westward direction, and (b) in the southeastward and northwestward direction.

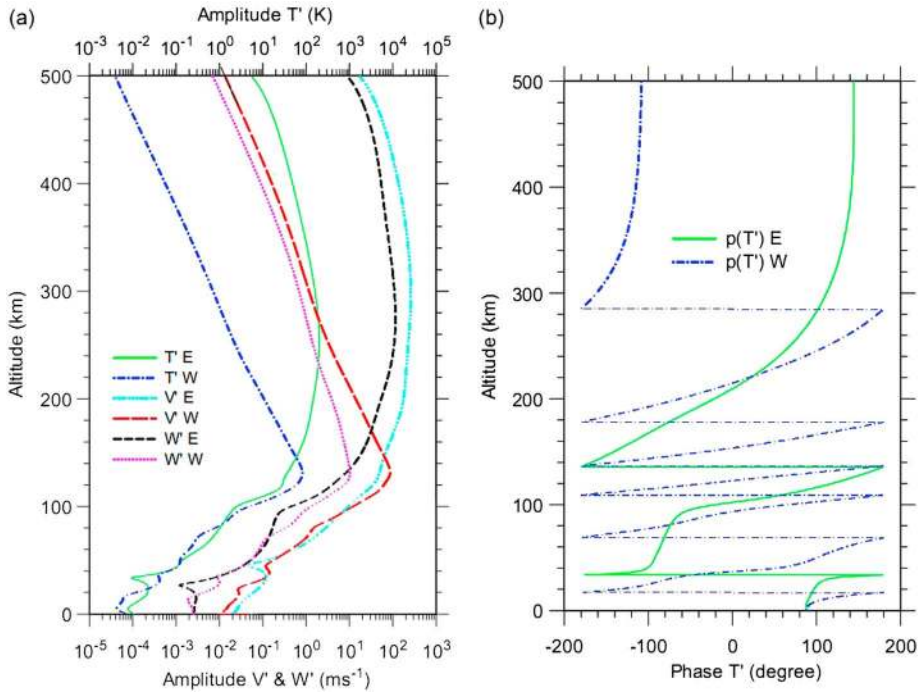

Figure 4. (a) Amplitudes of the temperature (upper x axis), zonal and vertical velocity perturbation (lower x axis), and (b) phases of the temperature perturbation for the 32 min waves propagating toward the east ($\lambda_h = 424.32$ km) and west ($\lambda_h = 232.32$ km), respectively.

($c = 221$ m/s) (Figure 3a) exhibits regions of evanescence ($m^2 < 0$) in the midtroposphere and to a lesser extent in the upper mesosphere. The wave becomes evanescent in the midtroposphere because in this region the wave is propagating into a zonal tail wind (Figure 1a) and its intrinsic phase speed approaches about 200 m/s, which exceeds about 0.54 of the local sound speed (c_{max}, the limiting speed for internal gravity waves, Figure 1b). In contrast, the westward propagating wave (Figure 3a, $c = 121$ m/s) is internally propagating everywhere ($m^2 > 0$). The southeastward propagating wave (Figure 3b, $c = 243$ m/s) also exhibits regions of evanescence ($m^2 < 0$) in the midtroposphere and in the upper mesosphere, but these regions are much broader in vertical extent due to the larger phase speed of this wave. Additionally, the wave becomes marginally evanescent in the lower mesosphere near 52 km altitude. The northwestward propagating gravity wave (Figure 3b, $c = 121$ m/s) remains internal everywhere. These results indicate that upward propagation should be partially impeded for the eastward and southeastward propagating waves due to limited regions of evanescence in the troposphere (associated with their intrinsic phase speeds exceeding about 0.54 of the local sound speed, c_{max}), and in the mesosphere. The westward and northwestward propagating waves do not experience evanescence and so their propagation to the lower thermosphere should occur relatively easily.

Figure 4 shows the full-wave model-derived perturbation amplitudes for the temperature, T', vertical velocity, W', and zonal velocity, V' (Figure 4a), and the phases of the temperature perturbation (Figure 4b). The temperature perturbation amplitudes for the eastward and westward propagating waves tend to grow with increasing height up to 120 km altitude. Undulations in the amplitudes seen below this height are mainly associated with partial reflections from regions of evanescence (for the eastward propagating wave), although weaker undulations are also present for the westward propagating wave associated with weak reflections from the base of the thermosphere. At thermospheric heights, the slower westward wave experiences a larger viscous dissipation rate than does the faster eastward propagating wave. At these heights the zonal wind is westward (Figure 1a), which accentuates this (through Doppler shifting) by decreasing the intrinsic phase speed of the slower (westward) wave and increasing the intrinsic phase speed of the faster (eastward) wave. The result is that the westward propagating wave has a shortened vertical wavelength, which increases the velocity shears and the associated viscous dissipation rate. Consequently,

although the westward propagating wave has a larger amplitude (80 K) than the eastward propagating wave (35 K) near 130 km altitude, the eastward propagating wave continues to grow in amplitude as it propagates upward into the higher thermosphere, and it achieves a maximum amplitude of about 200 K near 250 km altitude. In contrast, the westward propagating wave experiences strong dissipation in the thermosphere and its amplitude decreases substantially as it propagates further upward in the thermosphere.

The amplitudes of the zonal velocity perturbation (V') for the eastward and westward propagating waves are also shown in Figure 4a. For the westward propagating wave V' has a maximum value of about 85 m/s (centered near 130 km altitude in the *E* layer), larger than the value of about 50 m/s for V' due to the eastward propagation in this region. For the same reasons as discussed in the previous paragraph, V' continues to increase with increasing height in the thermosphere up to 300 km altitude for the eastward propagating wave, achieving a maximum value of about 260 m/s, while V' decreases rapidly with increasing height in the thermosphere for the westward propagating wave. The amplitudes of the vertical velocity (W') fluctuation for the eastward and westward propagating waves are also shown in this figure. Their variations with altitude closely follow those for the corresponding variations of V', but they are typically an order of magnitude smaller than V'.

Note that for the eastward propagating wave, a maximum temperature amplitude is about 200 K near 250 km altitude, approximately 21% of the mean (~950 K) at this altitude (see Figure 1b). The corresponding value of the horizontal velocity fluctuation amplitude is about 260 m/s. Although this amplitude is large, it is below the threshold amplitude required for the onset of convective instability. The *Orlanski and Bryan* [1969] criterion for the onset of convective instability is that $U' > c$ where U' is the horizontal wind perturbation and c is the intrinsic horizontal phase speed. For this wave, its intrinsic phase speed is equal to the extrinsic phase speed minus the zonal wind speed ($c - \underline{V} = 221 - (-90) = \sim 311$ m/s at 300 km altitude, Figure 1a), which is greater than the maximum value of U' (~260 m/s) at 300 km altitude. Because $U' < c$, the wave is stable to convective instability.

The phase of the temperature perturbation for wave propagation toward the east and west is shown as a function of height in Figure 4b. While the phase varies smoothly with height for the westward propagating wave, the phase for the eastward propagating wave is seen to undergo an almost discontinuous change in phase of π near 35 km altitude. It occurs slightly above the region of strong evanescence in the troposphere and below a region of slightly weaker evanescence in the upper mesosphere (Figure 3a). For the eastward propagating wave, weak standing wave behavior is noticeable in the phase variations below about 90 km altitude associated with these two regions of evanescence. The standing wave signature is also evident in the amplitude variations (weak nodes and antinodes) shown previously in Figure 4a. The westward propagating wave is slower and therefore has a shorter vertical wavelength (λ_z) than the eastward propagating wave. As noted previously, the shorter vertical wavelengths result in an increase in the velocity shears and subsequently an increase in the viscous dissipation rate. Above about 120 km altitude, the increase with increasing height of the Brunt-Väisälä period (Figure 1b) leads to an increase of the vertical wavelength for both the eastward and westward propagating waves. The molecular viscosity and thermal diffusivity affect wave amplitudes and phases, more so at great thermospheric heights where they become extremely large (Figure A2). The rapid diffusion of heat and momentum causes a "smearing" of the wave variations in the vertical, increasing the vertical wavelengths such that the waves are approaching evanescence by 500 km altitude (as revealed by the constant phase at great heights seen in Figure 4b).

The altitude variations of the temperature, horizontal, and vertical velocity fluctuation amplitudes derived from the full-wave model for the southeastward and northwestward propagating waves are shown in Figure 5a. At greater heights, the northwestward propagating wave experiences greater viscous dissipation than the southeastward propagating wave, with the result that the temperature perturbation amplitudes are considerably smaller at great thermospheric heights for the northwestward propagating wave. The horizontal velocity perturbation for the northwestward propagating wave has a maximum value of about 140 m/s at 150 km altitude, while that for the southeastward propagation is about half of this value at the same altitude. However, the faster, southeastward propagating wave with its larger vertical wavelength experiences less viscous dissipation than its northwestward propagating counterpart, and its amplitude continues to grow to about 225 m/s near 300 km altitude. The altitude variations of the vertical velocity fluctuation closely mimic those of the horizontal velocity perturbation, but they are typically an order of magnitude smaller than the latter.

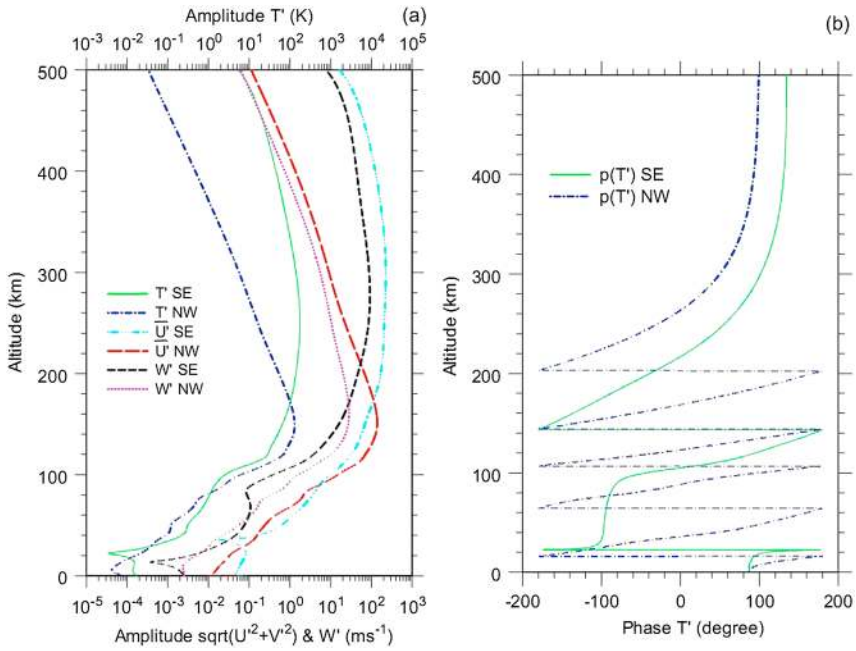

Figure 5. (a) Amplitudes of the temperature (upper *x* axis), horizontal and vertical velocity perturbation (lower *x* axis), and (b) phases of the temperature perturbation for the 32 min waves propagating toward the southeast ($\lambda_h = 466.56$ km) and northwest ($\lambda_h = 232.32$ km), respectively.

The phase variations of the temperature perturbation for the southeastward and northwestward propagating waves derived from the full-wave model are shown in Figure 5b. The faster southeastward propagating wave experiences strong evanescence in the middle troposphere and also in the upper mesosphere (Figure 3b), leading to fairly strong standing wave behavior below about 90 km altitude and a strong, discontinuous phase change of π near 20 km altitude. The northwestward propagating wave is slower (shorter λ_z) than the southeastward propagating wave, and so it experiences a greater viscous damping at higher altitudes than the faster southeastward propagating wave. Both waves are approaching evanescence by 500 km altitude (constant phase, Figure 5b).

In Figure 6, we show the variations with time and height of the vertical flux of wave horizontal momentum (the so-called Reynold's stress, defined as $F_M = \rho_0 \overline{u'w'}$, where the overbar denotes a horizontal average), which are derived from the 2-D time-dependent model. Results are presented for the 32 min wave packet propagating toward the northwest (Figure 6a), east (Figure 6b), west (Figure 6c), and southeast (Figure 6d), respectively. Note that in each case the lower boundary forcing is described by equation (1), but the wave horizontal wavelength (or phase speed) is different. Analysis of the vertical flux of the horizontal momentum carried by the waves is useful in simulation studies of the momentum forcing of the mean state due to the dissipation of wave packets [e.g., *Hickey et al.*, 2010b; *Liu et al.*, 2013]. Additionally, radar observations allow the momentum flux to be directly inferred from measured wind fluctuations and from correlations between the horizontal and vertical velocities [e.g., *Fritts and Yuan*, 1989]. Note that the energy flux has also previously been used to characterize the upward propagation of a gravity wave packet [*Yu and Hickey*, 2007a, 2007c].

The overall upward momentum fluxes for wave propagation toward the northwest (Figure 6a) and west (Figure 6c) are noticeably larger than those associated with wave propagation toward the southeast (Figure 6d) and east (Figure 6b). In addition, a comparison of Figures 6a and 6c shows that the gravity wave momentum fluxes associated with waves propagating toward the northwest are moderately larger than those associated with waves propagating toward the west. Gravity waves propagating toward the west and northwest both encounter head winds over a fairly broad region of the atmosphere centered near 60 km altitude during their upward propagation (Figure 1a). In this region, they will be Doppler shifted to higher frequencies, refracting the waves further upward, and increasing the upward momentum

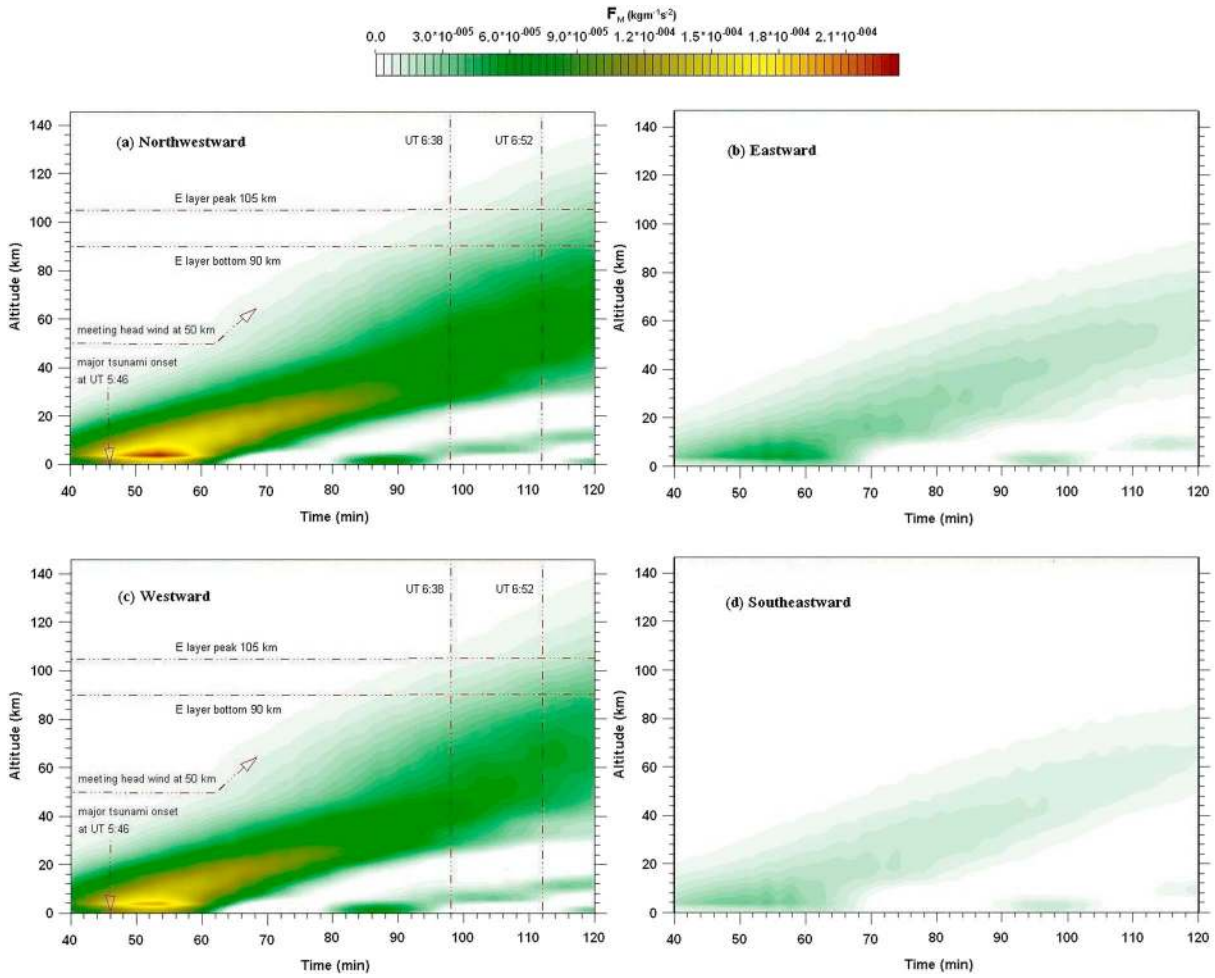

Figure 6. Time-height section of the vertical flux of the horizontal momentum (positive upward) for the 32 min wave packet propagating toward the (a) northwest (λ_h = 232.32 km), (b) east (λ_h = 424.32 km), (c) west (λ_h = 232.32 km), and (d) southeast (λ_h = 466.56 km), respectively.

fluxes (this is indicated in Figures 6a and 6c by the arrows appearing near 50 km altitude and a time of about 62 min). The leading (faster) components of the disturbance reach 90 and 105 km altitude at about UT 06:38 and UT 06:52, respectively, as indicated by the intersecting dashed lines shown in Figures 6a and 6c. These arrival times are in good agreement with those presented by *Galvan et al*. [2012], as shown in their Figures 2d (for 06:38:45 UT) and 2e (for 06:52:15 UT). This agreement provides a plausible explanation for the GPS-derived TEC observations, which showed that the most intense disturbances occurred in the westward and northwestward directions from the epicenter at the times.

5. Discussion

We have modeled the 2011 Tohoku tsunami as a deformation of our model lower boundary described by a modified Gaussian function with a maximum vertical displacement of 76 cm and traveling at a shallow-water wave speed that is a function of the ocean depth. The shallow-water wave speeds that we assume (based on DART data) are 121 m/s for westward and northwestward propagation, 221 m/s for eastward propagation, and 243 m/s for southeastward propagation. We have investigated the atmospheric gravity waves that this would produce and their propagation characteristics in a windy and viscous atmosphere for different directions of propagation. The faster eastward propagating gravity waves are able to propagate to *F* region heights, while the slower westward propagating gravity waves are viscously damped and achieve maximum amplitudes well below 200 km altitude. However, the westward propagating waves reach the lower thermosphere earlier (within an hour) and with larger amplitudes than the eastward propagating

waves, mainly due to the fact that the eastward propagating waves encounter regions of evanescence (or quasi-evanescence) throughout much of the lower and middle atmosphere.

We have calculated the vertical group speed using the full-wave model (and also using the dispersion relation of *Einaudi and Hines* [1971]) and compared the travel times with those inferred from the 2-D model results shown in Figure 6. For the westward propagating gravity wave of period 32 min, the largest value of the vertical group speed is about 28 m/s and occurs near 64 km altitude in a region of strong headwinds. Its average value between the sea surface and an altitude of 100 km is about 23 m/s (~65 min to reach 90 km altitude). However, the short period components of the wave packet shown in Figure 2 will have faster phase speeds and also faster group speeds. Hence, the faster (short period) part of the packet will arrive first. For a period of 25 min (where there is significant power), the largest value of the vertical group speed for the westward propagating gravity wave is about 32 m/s and occurs near 60 km altitude in a region of strong headwinds. Its average value between 0 and 100 km altitude exceeds 32 m/s (~47 min to reach 90 km altitude). These group speeds lead to propagation times (not shown here) that are consistent with the 2-D simulation results for the westward and northwestward propagating waves presented in Figures 6c and 6a, respectively, which are also consistent with the observations reported by *Galvan et al*. [2012].

It is also interesting to compare the vertical group speeds for the westward propagating waves with those for the eastward propagating waves. For the 25 min eastward propagating wave, the average vertical group speed is 21 m/s, while for the 32 min wave it is far less than 20 m/s. Hence, although the eastward propagating wave has a higher extrinsic phase speed (221 m/s) than the westward propagating wave (121 m/s), the winds profoundly affect their vertical group speeds (as well as on the refractive indexes for these waves, as shown in Figure 3a) and cause the westward propagating wave to reach the lower thermosphere far sooner than the eastward propagating wave. A similar reasoning also applies to the pair of the waves propagating toward the northwest and southeast. This result is also borne out by the 2-D model results and the observations of *Galvan et al*. [2012].

We note that our results have also shown that the eastward propagating waves will dominate in the middle and upper thermosphere primarily due to the effects of molecular viscosity and thermal conductivity, which preferentially damp the westward propagating waves. This should lead to an observable *F* region ionospheric response to the gravity wave forcing [e.g., *Occhipinti et al*., 2008; *Hickey et al*., 2009], but the propagation time to these altitudes should be almost two hours, which extends beyond the observations reported by *Galvan et al*. [2012].

Our choice of tsunami parameters is intended to provide a plausible packet of atmospheric gravity waves that propagate obliquely upward and outward from the epicenter, emanating from the ocean surface. There are two major sides from the epicenter which is located on the North American Plate. One may be on the directions toward the nearest coast line of Japan (toward the west and northwest); the other could be the directions toward the Japan Trench in the deep ocean (toward the east and southeast). Wave packets are allowed to travel with different shallow-water wave speeds ($\sqrt{gh}$) depending on their directions of propagation (and associated average ocean depths around the epicenter). The average ocean depths toward the north and south are quite flat, significantly less than those toward the deep ocean, and close to those toward the shallow coastal waters of Japan. Subject to the effects of the small meridional wind (below 100 km altitude, Figure 1a), their associated wave packets are propagating freely and obliquely upward (not shown here), but not appearing as intense and fast as their counterpart pairs of the westward and northwestward waves due to their relatively small wave phase speeds.

More recently, *Hickey et al*. [2009, 2010a] included several important physical processes that would significantly influence the ionospheric response to the 2004 Sumatra tsunami. In the paper, we have chosen to address the damping associated with molecular viscosity and thermal conduction, and the effects of background mean winds. We do not include composition effects in the thermosphere associated with altitude variations of the mean molecular weight [*Walterscheid and Hickey*, 2001, 2012] but note that these effects can be important for most gravity waves. These effects will be considered in future work, but are not expected to alter the conclusions of our present work concentrating on the lower thermosphere and *E* region ionosphere. The Coriolis force (owing to the rotation of the Earth) is neglected for the fairly short gravity wave period (compared to the 24 h diurnal period) that is considered here.

6. Conclusions

We have used two numerical models describing the propagation of atmospheric gravity waves that would likely be generated by the 2011 Tohoku tsunami in order to investigate the effects of ocean depth on these waves and on their propagation characteristics. We find that because the ocean depth lying to the east of the source of the tsunami (the earthquake epicenter) is deeper than that lying to the west, the eastward propagating gravity waves will be faster than the westward propagating gravity waves. In spite of this, we have found that the westward propagating gravity waves propagate faster and with larger amplitudes upward to the lower thermosphere in comparison to the eastward propagating waves. Our result that the initially observed gravity waves have a predominant westward direction of propagation is supported by the recent ionospheric observations of *Galvan et al*. [2012]. We also note that the plausible suggestion of *Galvan et al*. [2012] that the westward propagating atmospheric disturbance would be enhanced due to the amplification of the tsunami as it travels into shallower seas would augment the effects that we have described here. Although not the main subject of this study, we also find that the eastward propagating gravity waves would dominate in the middle thermosphere, but the propagation time to those altitudes would be a few hours after the tsunami onset.

Because gravity waves propagating toward the west or northwest are propagating against the mean flow, they will have a greater vertical group velocity and, therefore, reach the lower thermosphere sooner than eastward propagating waves. Hence, observations of this region should first see the westward (and northwestward) propagating disturbance. This modeling result is reconciled by the GPS TEC observations of *Galvan et al*. [2012] who, using the GEONET, showed that the initial atmospheric response was for the northwestward propagating waves.

Appendix A

A1. Two-Dimensional Time-Dependent Model

The neutral atmosphere is treated as a well-mixed, single-constituent gas. A dynamics model with highly coupled Navier-Stokes equations is used to describe 2-D, nonlinear, time-dependent, and nonhydrostatic plane wave motions. Lateral boundaries of the model are periodic over a horizontal wavelength to simulate a horizontally infinite domain. As a consequence of the mechanism of the ocean-atmosphere coupling, the variation of the vertical velocity induced by the vertical displacement of the ocean surface serves as a lower boundary forcing in a nonisothermal, viscous atmosphere and in the presence of background winds. The prescribed forcing by the 2011 Tohoku tsunami (discussed in section 3) is in association with the geographic information shown in Figure A1. The tsunamigenic gravity wave propagation can be described using the Navier-Stokes equations for flow without rotation.

A time-splitting technique is applied to the finite difference equations that are derived from the Navier-Stokes equations. The time integration for these highly coupled nonlinear equations is performed using an explicit second order Lax-Wendroff scheme and an implicit iterative Newton-Raphson scheme. A thorough explanation of the model configuration, such as the discretization schemes and computational algorithms, is beyond the scope of our present introduction but can be found in the works of *Yu et al*. [2009]. A similar numerical approach has also been used by *Walterscheid and Schubert* [1990]. The model has previously been used to elucidate the temporal evolution of the wave vertical energy flux [*Yu and Hickey*, 2007a, 2007c] and thermospheric thermal ducting [*Yu and Hickey*, 2007b].

$$\rho\frac{D\underline{v}}{Dt}+\underline{\nabla}p-\rho\underline{g}-\underline{\nabla}\cdot(\rho\upsilon\underline{\nabla}\underline{v})-\underline{\nabla}\cdot(\rho\eta_e\underline{\nabla}\underline{v})+\rho K_R\underline{v}=\rho\left(\frac{D^2\underline{Z}}{Dt^2}\right), \tag{A1}$$

$$\rho c_v\frac{DT}{Dt}+p\underline{\nabla}\cdot\underline{v}-\underline{\nabla}\cdot(\lambda_m\underline{\nabla}T)-\frac{c_pT}{\theta}\underline{\nabla}\cdot(\rho\kappa_e\underline{\nabla}\theta)+c_v\rho K_NT=0. \tag{A2}$$

With the exception for the equation of state for an ideal gas, the definition of potential temperature, and the equation for conservation of mass (all not shown), we provide the momentum (A1) and energy (A2) equations here in order to analyze the viscosity and thermal conduction due to eddy and molecular processes. The operator $D/Dt=\partial/\partial t+\underline{v}\cdot\underline{\nabla}$ is the substantial derivative, where $\underline{v}$ (x, z, t) is the total velocity vector (mean plus perturbation); $\underline{Z}$ (0, ξ) is the displacement vector on the ocean surface and is a function

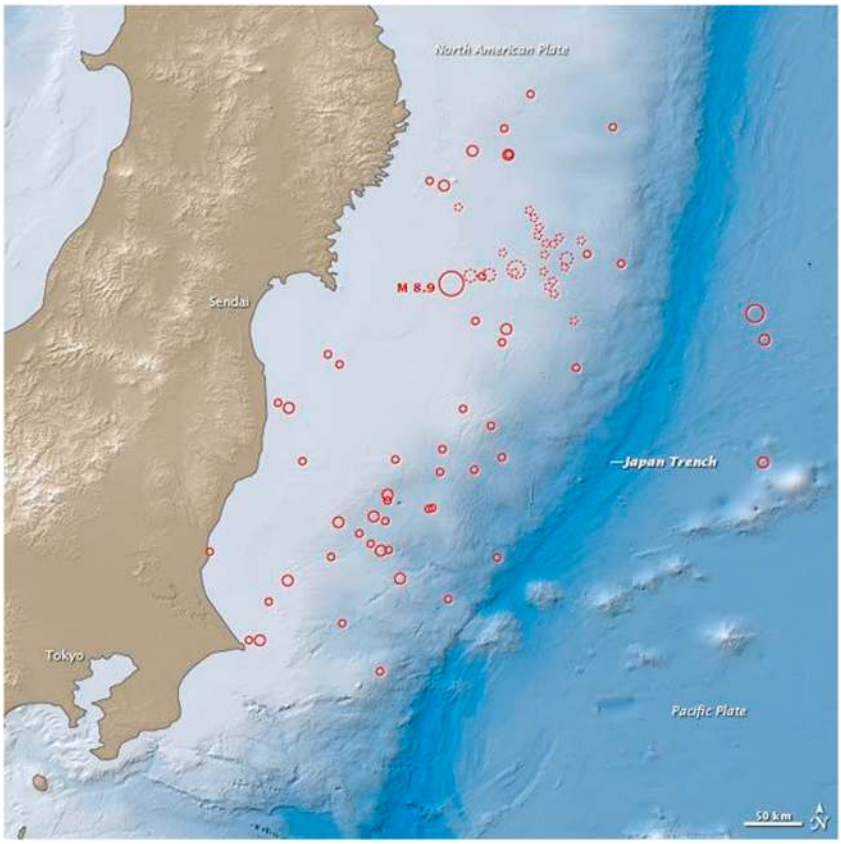

Figure A1. Map showing the location of the epicenter (38.322°N, 142.369°E) of the earthquake (*M* 8.9) responsible for the 2011 Tohoku tsunami.

of the vertical coordinate, ξ (x, 0, t), which is a function of the horizontal position (x) and time (t) (and defined in equation (1) of the main text); ρ is the atmospheric neutral density; p is the atmospheric pressure; T is the atmospheric temperature; θ is the potential temperature; g is the acceleration due to gravity; υ is the molecular viscosity; η_e is the eddy momentum diffusivity; c_v and c_p are the specific heats at constant volume and constant pressure, respectively; λ_m is the molecular thermal conductivity; κ_e is the eddy thermal diffusivity; and K_R and K_N are Rayleigh friction and Newtonian cooling coefficients, respectively.

A2. Viscosity Effects

The molecular diffusion coefficients used in the momentum (A1) and energy (A2) equations are basically taken from the book written by *Rees* [1989]. In a dissipative atmosphere, we apply molecular processes involving molecular kinematic viscosity υ (units in $m^2\,s^{-1}$), which can be numerically expressed as follows [*Hickey and Yu*, 2005]

$$\upsilon = \frac{[N_2]\times 3.43 + [O_2]\times 4.03 + [O]\times 3.90}{\rho_0 \times ([N_2]+[O_2]+[O])} \times (T_0)^{0.69} \times 10^{-7}. \tag{A3}$$

Brackets [] in the equation denote the number density for the major or minor species. The term ρ_0 is the atmospheric mean density; T_0 is the atmospheric mean temperature. They are both functions of altitude. Another molecular process is due to the molecular thermal conductivity, λ_m, that can be numerically expressed as follows [*Hickey and Yu*, 2005]

$$\lambda_m = \frac{[N_2]\times 56.0 + [O_2]\times 56.0 + [O]\times 75.90}{([N_2]+[O_2]+[O])} \times (T_0)^{0.69} \times 10^{-5}, \tag{A4}$$

and it is plotted in Figure A2 as $\lambda_m/\rho c_v$ (units in $m^2\,s^{-1}$).

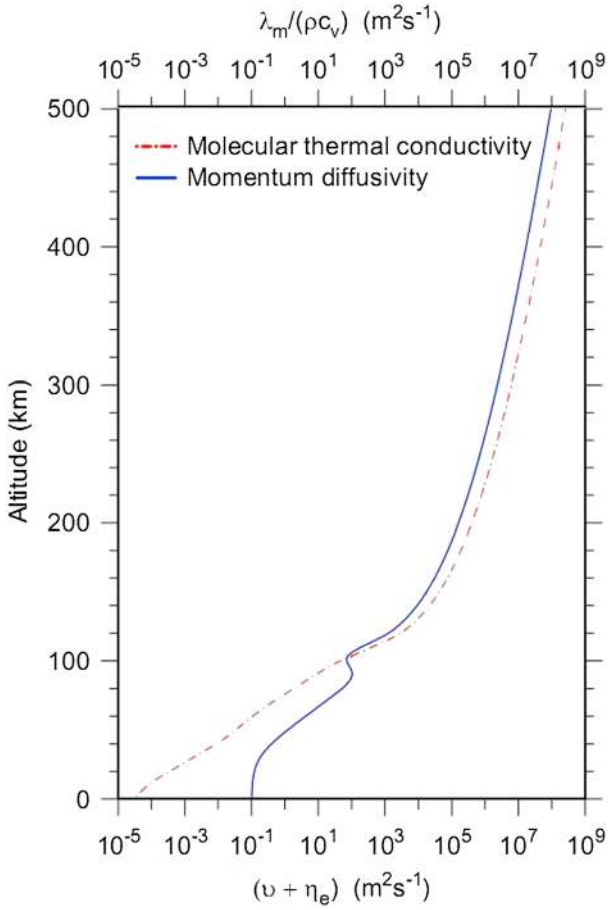

Figure A2. The molecular thermal conductivity (dashed dotted line, $\lambda_m/\rho c_v$) and momentum diffusivity (solid line, $\upsilon + \eta_e$).

The nominal eddy diffusion coefficients are generally based on a profile due to *Strobel* [1989] and have large values in the mesopause region. The eddy momentum diffusivity maximizes with a value of $100\,m^2\,s^{-1}$ at 90 km altitude. This maximum value for the eddy diffusivity is comparable to values derived from radar inferences of the turbulent energy dissipation rates [*Hocking*, 1987]. Similar values have also been derived from 2 years of continuous radar measurements near Adelaide, Australia [*Hocking*, 1988]. A small value of eddy diffusivity ($0.1\,m^2\,s^{-1}$) is used for the lower atmosphere below 50 km altitude. Eddy diffusion processes involve the eddy momentum diffusivity that is numerically expressed as follows [*Hickey and Yu*, 2005]

$$\eta_e = 100\,\mathrm{sech}(2.6 \times (z(\mathrm{km}) - 90.0)/20) + 0.1. \quad \text{(A5)}$$

Another eddy diffusion process is due to the eddy thermal diffusivity $\kappa_e = \eta_e/3$ (units in $m^2\,s^{-1}$), where we have considered a Prandtl number of 3.

The altitude variations of the viscosity and thermal conductivity are plotted in Figure A2. The viscosity comprises the molecular kinematic viscosity, υ, plus the eddy momentum diffusivity, η_e ($\upsilon + \eta_e$, units in $m^2\,s^{-1}$). Although the thermal diffusivity includes the molecular thermal conductivity (λ_m) and the eddy thermal diffusivity (κ_e), for clarity we do not include the latter in this figure (κ_e exhibits a similar variation with altitude as η_e). The momentum diffusivity profile has an eddy diffusion component that maximizes at 90 km altitude with a value of $100\,m^2/s$. At greater heights, the molecular viscosity dominates over the eddy diffusivity (likewise, the molecular thermal conductivity dominates over the eddy thermal diffusivity at these heights). The molecular viscosity and thermal conductivity (scaled by a factor of ρc_v) both increase smoothly with increasing altitude to values of about 10^8 and $2.6 \times 10^8\,m^2/s$, respectively, by 500 km altitude. The significant increase in the molecular diffusion with increasing altitude means that acoustic-gravity waves are more severely dissipated at higher thermospheric altitudes.

Acknowledgments

Yonghui Yu was supported by the National Natural Science Foundation of China under grants 40874100 and 41174128 to Nanjing University of Aeronautics and Astronautics. Michael P. Hickey was supported by the U.S. NSF grant AGS-1001074. Data generated by models supporting this article are available to readers who could request from the above authors.

Michael W. Liemohn thanks Zhiguo Deng and another reviewer for their assistance in evaluating this paper.

References

Artru, J., V. Ducic, H. Kanamori, P. Lognonne, and M. Murakami (2005a), Ionospheric detection of gravity waves induced by tsunamis, *Geophys. J. Int.*, *160*, 840–848.

Artru, J., P. Lognonne, G. Occhipinti, F. Crespon, R. Garcia, E. Jeansou, and M. Murakami (2005b), Tsunami detection in the ionosphere, *Space Res. Today*, *163*, 23–27.

Einaudi, F., and C. O. Hines (1971), WKB approximation in application to acoustic-gravity waves, *Can. J. Phys.*, *48*, 1458–1471.

Fritts, D. C., and L. Yuan (1989), Measurement of momentum fluxes near the summer mesopause at Poker Flat, Alaska, *J. Atmos. Sci.*, *46*, 2569–2579.

Galvan, D. A., A. Komjathy, M. P. Hickey, P. Stephens, J. Snively, Y. Tony Song, M. D. Butala, and A. J. Mannucci (2012), Ionospheric signatures of Tohoku-Oki tsunami of March 11, 2011: Model comparisons near the epicenter, *Radio Sci.*, *47*, RS4003, doi:10.1029/2012RS005023.

Hedin, A. E. (1991), Extension of the MSIS thermosphere model into the middle and lower atmosphere, *J. Geophys. Res.*, *96*, 1159–1172, doi:10.1029/90JA02125.

Hedin, A. E., et al. (1996), Empirical wind model for the upper, middle and lower atmosphere, *J. Atmos. Terr. Phys.*, *58*, 1421–1447.

Hickey, M. P., and Y. Yu (2005), A full-wave investigation of the use of a "cancellation factor" in gravity wave-OH airglow interaction studies, *J. Geophys. Res.*, *110*, A01301, doi:10.1029/2003JA010372.

Hickey, M. P., R. L. Walterscheid, M. J. Taylor, W. Ward, G. Schubert, Q. Zhou, F. Garcia, M. C. Kelley, and G. G. Shepherd (1997), Numerical simulations of gravity waves imaged over Arecibo during the 10-day January 1993 Campaign, *J. Geophys. Res.*, *102*(A6), 11,475–11,490, doi:10.1029/97JA00181.

Hickey, M. P., G. Schubert, and R. L. Walterscheid (2009), Propagation of tsunami-driven gravity waves into the thermosphere and ionosphere, *J. Geophys. Res.*, *114*, A08304, doi:10.1029/2009JA014105.

Hickey, M. P., G. Schubert, and R. L. Walterscheid (2010a), Atmospheric airglow fluctuations due to a tsunami-driven gravity wave disturbance, *J. Geophys. Res.*, *115*, A06308, doi:10.1029/2009JA014977.

Hickey, M. P., R. L. Walterscheid, and G. Schubert (2010b), Wave mean flow interactions in the thermosphere induced by a major tsunami, *J. Geophys. Res.*, *115*, A09309, doi:10.1029/2009JA014927.

Hines, C. O. (1972), Gravity waves in the atmosphere, *Nature*, *239*, 73–78.

Hocking, W. K. (1987), Turbulence in the region 80–120 km, *Adv. Space Res.*, *7*(10), 171–181.

Hocking, W. K. (1988), Two years of continuous measurements of turbulence parameters in the upper mesosphere and lower thermosphere made with a 2-MHz radar, *J. Geophys. Res.*, *93*, 2475–2491, doi:10.1029/JD093iD03p02475.

Komjathy, A., D. A. Galvan, P. Stephens, M. Butala, V. Akopian, B. Wilson, O. Verkhoglyadova, A. Mannucci, and M. P. Hickey (2012), Detecting ionospheric TEC perturbations caused by natural hazards using a global network of GPS receivers: The Tohoku case study, *Earth Planets Space*, *64*, 1–8.

Liu, X., J. Xu, J. Yue, and S. L. Vadas (2013), Numerical modeling study of the momentum deposition of small amplitude gravity waves in the thermosphere, *Ann. Geophys.*, *31*, 1–14, doi:10.5194/angeo-31-1-2013.

Occhipinti, G. E., A. Kherani, and P. Lognonne (2008), Geomagnetic dependence of ionospheric disturbances induced by tsunamigenic internal gravity waves, *Geophys. J. Int.*, *173*, 753–765.

Orlanski, I., and K. Bryan (1969), Formation of the thermocline step structure by large-amplitude internal gravity waves, *J. Geophys. Res.*, *74*, 6975–6983, doi:10.1029/JC074i028p06975.

Peltier, W. R., and C. O. Hines (1976), On the possible detection of tsunamis by a monitoring of the ionosphere, *J. Geophys. Res.*, *81*, 1995–2000, doi:10.1029/JC081i012p01995.

Rees, M. H. (1989), *Physics and Chemistry of the Upper Atmosphere*, Cambridge Univ. Press, New York.

Strobel, D. F. (1989), Constraints on gravity wave induced diffusion in the middle atmosphere, *Pure Appl. Geophys.*, *130*, 533–546.

Walterscheid, R. L., and G. Schubert (1990), Nonlinear evolution of an upward propagating gravity wave: Overturning, convection, transience and turbulence, *J. Atmos. Sci.*, *47*(1), 101–125.

Walterscheid, R. L., and M. P. Hickey (2001), One-gas models with height-dependent mean molecular weight: Effects on gravity wave propagation, *J. Geophys. Res.*, *106*, 28,831–28,839, doi:10.1029/2001JA000102.

Walterscheid, R. L., and M. P. Hickey (2011), Group velocity and energy flux in the thermosphere: Limits on the validity of group velocity in a viscous atmosphere, *J. Geophys. Res.*, *116*, D12101, doi:10.1029/2010JD014987.

Walterscheid, R. L., and M. P. Hickey (2012), Gravity wave propagation in a diffusively separated gas: Effects on the total gas, *J. Geophys. Res.*, *117*, A05303, doi:10.1029/2011JA017451.

Yu, Y., and M. P. Hickey (2007a), Time-resolved ducting of atmospheric acoustic-gravity waves by analysis of the vertical energy flux, *Geophys. Res. Lett.*, *34*, L02821, doi:10.1029/2006GL028299.

Yu, Y., and M. P. Hickey (2007b), Numerical modeling of a gravity wave packet ducted by the thermal structure of the atmosphere, *J. Geophys. Res.*, *112*, A06308, doi:10.1029/2006JA012092.

Yu, Y., and M. P. Hickey (2007c), Simulated ducting of high-frequency atmospheric gravity waves in the presence of background winds, *Geophys. Res. Lett.*, *34*, L11103, doi:10.1029/2007GL029591.

Yu, Y., M. P. Hickey, and Y. Liu (2009), A numerical model characterizing internal gravity wave propagation into the upper atmosphere, *Adv. Space Res.*, *44*(7), 836–846.